

Charge dynamics in the phase string model for high- T_c superconductors

Zheng-Cheng Gu and Zheng-Yu Weng

Center for Advanced Study, Tsinghua University, Beijing 100084

(Dated: February 6, 2008)

An understanding of the anomalous charge dynamics in the high- T_c cuprates is obtained based on a model study of doped Mott insulators. The high-temperature optical conductivity is found to generally have a two-component structure: a Drude like part followed by a mid-infrared band. The scattering rate associated with the Drude part exhibits a linear-temperature dependence over a wide range of high temperature, while the Drude term gets progressively suppressed below a characteristic energy of *magnetic* origin as the system enters the pseudogap phase. The high-energy optical conductivity shows a resonancelike feature in an underdoped case and continuously evolves into a $1/\omega$ tail at higher doping, indicating that they share the same physical origin. In particular, such a high-energy component is closely correlated with the ω -peak structure of the density-density correlation function at *different* momenta, in systematic consistency with exact diagonalization results based on the t - J model. The underlying physics is attributed to the *high-energy* spin-charge separation in the model, in which the “mode coupling” responsible for the anomalous charge properties is *not* between the electrons and some collective mode but rather between new charge carriers, holons, and a novel topological gauge field controlled by spin dynamics, as the consequence of the strong short-range electron-electron Coulomb repulsion in the doped Mott insulator.

PACS numbers: 74.20.Mn, 72.10.-d, 74.25.Gz, 78.20.Bh

I. INTRODUCTION

Charge dynamics in the high- T_c cuprates has been under intensive studies for nearly two decades by now. With the continuous improvements in experimental techniques and sample quality, the anomalous charge dynamics exhibited in optical measurements has been firmly established as intrinsic properties unique to the high- T_c cuprates.

Some important features observed^{1,2} in the in-plane optical measurements are: (a) The undoped parent compound is a Mott insulator with a clear charge transfer gap observed in the optical conductivity. Upon doping, spectral weight starts to appear inside the charge transfer gap.³ (b) In heavily underdoped materials, the optical conductivity shows a very clear two-component feature: a low-lying Drude component followed by a resonancelike peak around the so-called high mid-infrared energy $\omega_{\text{mir}}^H \sim 0.5 - 0.8$ eV.³⁻⁶ (c) Below some pseudogap temperature in the underdoped cuprates, the low-energy part of the optical conductivity is suppressed with decreasing temperature, accompanied by an emerging *lower* mid-infrared resonancelike peak at ω_{mir}^L (~ 0.1 eV near the optimal case).^{6,7} (d) Near the optimal doping, the high mid-infrared peak around ω_{mir}^H continuously evolves into an approximate $1/\omega$ behavior in the optical conductivity, with a shift of spectral weight towards lower energy.^{5,8} At the same time, the scattering rate shows a linear- ω dependence,^{9,10} while the scattering rate at $\omega \sim 0$ increases linearly with temperature, consistent with the dc resistivity measurement.¹¹⁻¹³

Such anomalous electromagnetic response in the cuprates has posed a great challenge to any microscopic theory with regard to the charge scattering mechanism. Mainly focusing on the optimal case, the one-component approaches, including the marginal Fermi-liquid theory,¹⁴ projected Fermi liquid with edge singularities,¹⁵ slave-boson gauge theory,¹⁶ nearly antiferromagnetic Fermi-liquid theory,^{17,18} etc., have all stressed how the scattering rate $1/\tau$ may become strongly frequency-dependent as the consequence of strong interactions. Conventional electron-boson-mode coupling mechanisms have been also suggested in this regard.¹⁹⁻²² Alternatively the power-law behavior of the scattering rate $1/\tau(\omega) \sim \omega^\alpha$ has also been interpreted as due to some zero-temperature quantum critical point hiding below the superconducting dome in the phase diagram.²⁶

To fit the underdoped data, however, a multi-component model composed of a free-carrier Drude term and a set of Lorentzian oscillators seems more appropriate based on a phenomenological consideration to account for the high mid-infrared band.^{1,2} Note that the presence of a mid-infrared band has been indeed found in various microscopic models describing the hole motion in a quantum antiferromagnet.²³⁻²⁵ On the other hand, numerical studies²⁷ based on the t - J model and Hubbard model have also shown the existence of a mid-infrared absorption at small doping and its evolution into an approximately $1/\omega$ tail with increasing doping. These all point to the fact that strong correlations may be essential in order to fully understand the overall charge dynamics in the cuprates.

In this paper, we will study the global feature of charge dynamics based on an effective theory describing a doped Mott insulator. Due to the strong correlation nature, the charge scattering mechanism is no longer a conventional mode coupling between the electrons and some collective bosonic mode. It is replaced by a new type of “mode coupling”,

in which the *spinless* charge carriers, holons, interact with a topological gauge field, with the latter controlled by the *neutral* spin dynamics. Namely the strong short-range Coulomb interaction effect between the electrons is now represented by a novel scattering between the charge and spin degrees of freedom of the system.

Base on this model, we show that the high-temperature optical conductivity is generically associated with a two-component behavior. Here the low- ω Drude-like term is characterized by a linear-temperature-dependent scattering rate over a wide range of temperature, which gets progressively suppressed as the system enters into the pseudogap phase at low temperature with the emerging of a lower mid-infrared peak. On the other hand, the high- ω mid-infrared part exhibits a resonancelike feature in the strong scattering case and continuously evolves into a $1/\omega$ tail in the weak scattering limit, which can be related to the underdoping and high doping, respectively. The high-energy mid-infrared component is further shown to be closely correlated with the ω -peak structure of the density-density correlation function at *different* momenta which is systematically consistent with the exact diagonalization results based on the t - J model. Therefore, we establish a consistent picture for the charge dynamics in the cuprate superconductors in different temperature and energy regimes within a *single* unified theoretical framework.

The rest of paper will be organized as follows. In Sec. II, the basic model describing a doped Mott insulator will be introduced, and various important temperature and energy scales decided by the model will be discussed. In particular, a novel charge scattering mechanism embedded in the model will be emphasized. In Sec. III, we study the high-temperature charge dynamics where the gauge fluctuations are reduced to static to allow for a numerical simulation. The optical conductivity and scattering rate are calculated. The two-component ω structure and its correlation with the density-density correlation function will be discussed in detail. In Sec. IV, the scattering strength is substantially reduced in the pseudogap phase where a perturbation approach is allowed to study the low-energy optical conductivity. A pseudogap behavior of the optical conductivity with the emergence of a lower mid-infrared resonance will be determined here. Finally, a summary and discussions will be presented in Sec. V.

II. BASIC MODEL

From a doped-Mott-insulator point of view, the t - J model is believed to be the simplest relevant model for the high- T_c cuprates. Finding the correct low-energy effective theory for the t - J model has been a fascinating focus in search for the mechanism of high- T_c superconductivity. The concepts of the resonating-valence-bond (RVB)²⁸ and spin-charge separation²⁹ have been conjectured in order to understand the strong correlation nature of the electrons in such a system, although, different from the one-dimensional case,^{30,31} no well-defined spinless charge carriers (holons) and $S = 1/2$ neutral spin excitations (spinons) have ever been unambiguously identified experimentally in the two-dimensional case. Nevertheless, there has been strong numerical evidence indicating that the charge and spin dynamics should be described separately by two different degrees of freedom with distinct characteristic energy scales.^{30,32}

Microscopic studies of the t - J model indicate that residual strong correlations still generally exist, in a spin-charge separation description, between the two building blocks – spinless “holons” and charge neutral “spinons”. For example, the interaction is mediated by the $U(1)$ ³³ or $SU(2)$ ³⁴ gauge field in the slave-boson approach. In contrast, in the phase string theory³⁵ the elementary force between the bosonic “holons” and “spinons” is mediated by the mutual Chern-Simons gauge fields. These gauge interactions complicate the issue regarding how to make a clear identification of holons and spinons, even if they exist in the cuprates.

Nevertheless, the presence of a spin-charge separation will predict a set of highly nontrivial charge and spin dynamics whose unique features can be subjected to a systematic comparison with the experimental measurement. Even in low-temperature phases where the confinement of “holons” and “spinons” due to the gauge fields may occur *at low energies*, the composite structure of the electrons in terms of “holons” and “spinons” should still exhibit interesting features with the increase of energy, which approaches the “asymptotic freedom” at some shorter distance and higher energy. An experimental probe of high-energy excitations is particularly meaningful here.

In the following, we explore the charge dynamics based on an effective gauge theory derived from the t - J model and show how the spin-charge separation exhibits and plays the essential role there.

A. Phase string model

Our starting point is the phase string model,^{35–37} which takes the form: $H_{\text{string}} = H_h + H_s$ with

$$H_h = -t_h \sum_{\langle ij \rangle} \left(e^{iA_{ij}^s + eA_{ij}^e} \right) h_i^\dagger h_j + H.c. + \lambda_h \sum_i (n_i^h - \delta) \quad (1)$$

$$H_s = -J_s \sum_{\langle ij \rangle \sigma} \left(e^{i\sigma A_{ij}^h} \right) b_{i\sigma}^\dagger b_{j-\sigma}^\dagger + H.c. + \lambda \sum_{i\sigma} [n_{i\sigma}^b - (1 - \delta)/2] \quad (2)$$

in which the holon field, described by the bosonic annihilation operator h_i , carries the full charge $+e$ coupling to the external electromagnetic vector potential A_{ij}^e .

The spinless holon field and the neutral $S = 1/2$ spinon field (which carries the spin index as described by the bosonic annihilation operator $b_{i\sigma}$) are minimally coupled to two internal gauge field A_{ij}^s and A_{ij}^h , whose gauge-invariant strengths are constrained to the matter fields by the following relations, respectively

$$\sum_C A_{ij}^s = \pi \sum_{l \in \Sigma_C} (n_{l\uparrow}^b - n_{l\downarrow}^b) \quad (3)$$

$$\sum_C A_{ij}^h = \pi \sum_{l \in \Sigma_C} n_l^h \quad (4)$$

where $n_{l\sigma}^b = b_{l\sigma}^\dagger b_{l\sigma}$ and $n_l^h = h_l^\dagger h_l$, respectively, denote the on-site spinon and holon number operators, and Σ_C is the region enclosed by an arbitrary (counterclockwise) closed loop C . Such relations are known as the mutual Chern-Simons gauge structure which dictate that a holon and a spinon perceive each other as a fictitious π -flux tube [here to avoid the short-distance uncertainty at each center of a π -flux tube, on the right-hand sides (rhs) of Eqs. (3) and (4), the distribution of a holon or spinon at site l should be understood as being slightly smeared within a small area centered at l].

The phase string model thus defined explicitly respects all the symmetries including the translational, time-reversal, parity, and spin rotational symmetries. Note that the spin operators in this model are defined by $S_i^z = 1/2 \sum_\sigma \sigma n_{i\sigma}^b$, $S_i^+ = b_{i\uparrow}^\dagger b_{i\downarrow} (-1)^i e^{i\Phi_i^h}$, and $S_i^- = (S_i^+)^^\dagger$, where $\Phi_i^h - \Phi_j^h = 2A_{ij}^h$ with the core of each flux-tube being smeared within a small area as mentioned above.

In Eqs. (3) and (4), λ_h and λ are the chemical potentials to implement $\sum_l n_l^h = N\delta$ and $\sum_{l\sigma} n_{l\sigma}^b = N(1-\delta) \equiv N\bar{n}^b$, where N is the total number of lattice sites and δ the doping concentration. The effective hopping integral $t_h \sim 0.67t^{37}$ and in this paper we shall choose $t_h = 2J$ which corresponds to $t \sim 3J$. The renormalized superexchange coupling $J_s = J \langle \hat{\Delta}^s \rangle (1 - 2g\delta)/2$ ($g \sim 2$)³⁸ with $J_s \sim J/2$ at low doping, where t and J are the bare parameters in the original t - J model. Here the gauge-invariant bosonic RVB order parameter $\Delta^s = \langle \hat{\Delta}^s \rangle \equiv \langle \sum_\sigma e^{-i\sigma A_{ij}^h} b_{i\sigma} b_{j-\sigma} \rangle$ is determined self-consistently.

B. Phase diagram and basic energy scales

Fig. 1 shows the basic phase diagram^{38,39} for the phase string model given in Eqs. (1) and (2). The characteristic temperature T_0 denotes the boundary of the so-called the upper pseudogap phase (UPP), described by the bosonic RVB order parameter $\Delta^s \neq 0$ based on H_s ;³⁸ The so-called lower pseudogap phase (LPP) or spontaneous vortex phase (SVP) is nested within the UPP with a characteristic temperature T_v , which corresponds to the bosonic degenerate regime for the holons;^{39,40} Finally the superconducting (SC) phase coherence is realized inside the LPP/SVP at lower temperatures. In Fig. 1 both LPP and SC phase terminate at half-filling where an antiferromagnetic (AF) long-range order is recovered in the ground state of H_s . Note that a more careful study with considering the longer-range AF correlations will lead to the vanishing of the SC transition temperature T_c at a finite critical doping concentration x_c .⁴¹

Physically the UPP is a regime where short-range AF correlations start to develop quickly with decreasing temperature.³⁸ At half-filling, it continuously evolves into the AF long-range ordered state at $T = 0$, where the gapless spin-wave excitation is shown in Fig. 2 by the dotted curve.⁴² However, such long-range AF correlations get “truncated” at finite doping after entering LPP, where an energy gap E_g is opened up around the AF wave vector $\mathbf{Q} = (\pi, \pi)$ as shown in Fig. 2, which depicts the peak positions of the spin dynamic susceptibility function $\text{Im}\chi^{zz}(\mathbf{q}, \omega)$ at $T = 0$ ⁴² (see Appendix A).

The doping dependence of the resonancelike spin energy E_g is illustrated in Fig. 1 which scales with T_c as $T_c \simeq E_g/4k_B$ as previously established⁴³ based on the phase string model. The peak structure of $\text{Im}\chi^{zz}(\mathbf{q}, \omega)$ in Fig. 2 coincides with the spin-wave spectrum at half-filling (dotted curve) and becomes a non-propagating mode with a finite, doping-dependent width in the momentum space at finite doping. But the overall high-energy envelop of the latter still well tracks that of the (softened) spin wave, implying that the short-range AF correlations remain strong in the short-distance, high-energy regime in the UPP. This is consistent with the neutron scattering measurements.⁴⁴ There is a characteristic *upper-bound* energy scale, E_s^{upper} , indicated by the arrows in Fig. 2 for the $S = 1$ excitations. Its doping dependence follows closely with T_0 in Fig. 1 and monotonically increases with reducing doping, reaching $E_s^{\text{upper}} \simeq 2.3J$ at half-filling.

The low-lying sharp resonancelike structure in $\text{Im}\chi^{zz}(\mathbf{q}, \omega)$ at E_g is the consequence⁴² of the *holon condensation* realized in H_h which then influences Eq. (2) via the gauge field A_{ij}^h in terms of Eq. (4). With the increase of

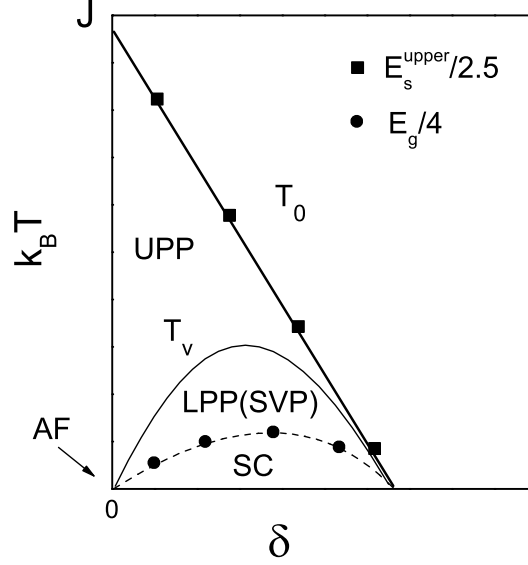


FIG. 1: In the phase diagram of the phase string model, the characteristic temperature T_0 for the upper pseudogap phase (UPP) and T_c for the superconducting phase (SC) are shown to be well scaled with two basic energy scales, E_s^{upper} and E_g (see Fig. 2 for their definitions), with the proportional coefficients ~ 0.4 and 0.25 , respectively. The lower pseudogap phase (LPP) or the spontaneous vortex phase (SVP) is characterized by a temperature T_v which is also determined by the spin excitation spectrum.³⁹

temperature, the holon condensation (or more precisely the amplitude condensation of the holon field) will terminate, not at T_c , but at an intermediate characteristic temperature scale T_v lying between T_0 and T_c that represents the onset of the LPP/SVP in Fig. 1. Such a bosonic degenerate regime corresponds to the Nernst regime observed in the cuprates.⁴⁵

C. Novel scattering mechanism

The charge dynamics is governed by H_h [Eq. (1)], in which a bosonic holon, carrying the full charge $+e$, will get scattered off by an internal gauge field A_{ij}^s . According to Eq. (3), an isolated spinon excitation will serve as a π -flux tube perceived by the holons and thus provides a strong, unconventional charge scattering source. So at high temperature when a lot of spinons are thermally excited, one expects a severe intrinsic frustration effect exerted from A_{ij}^s on the holons. On the other hand, the effect of the π -flux tubes bound to those spinons which are RVB paired at short-distance will be essentially cancelled out. At sufficiently low temperature and low energy where the majority of spins remain short-range RVB paired, the gauge fluctuations in A_{ij}^s will then be substantially reduced to result in a weak scattering, which warrants a perturbation treatment.

To see how the spin dynamics influences the charge degree of freedom via A_{ij}^s , one may introduce $\mathbf{A}^s \cdot (\mathbf{r}_i - \mathbf{r}_j) \equiv A_{ij}^s$ and express the propagator of the gauge field \mathbf{A}^s in the continuum limit as follows

$$\begin{aligned} D_{\alpha\beta}^{A^s}(\mathbf{q}, i\omega_n) &\equiv \int_0^\beta d\tau e^{i\omega_n \tau} \langle T_\tau A_\alpha^s(\mathbf{q}, \tau) A_\beta^s(-\mathbf{q}, 0) \rangle \\ &= - \left(\delta_{\alpha\beta} - \frac{q_\alpha q_\beta}{q^2} \right) \frac{4\pi^2}{q^2 a^4} \chi^{zz}(\mathbf{q}, i\omega_n) \end{aligned} \quad (5)$$

using Eq. (3), where $\chi^{zz}(\mathbf{q}, i\omega_n)$ is the \hat{z} -component spin susceptibility function.

The detailed spin dynamics described by H_s in Eq. (2) has been systematically studied^{38,42} before. For example, the peak structure in $\text{Im}\chi^{zz}(\mathbf{q}, \omega)$ at the mean-field level⁴² ($T = 0$) is presented in Fig. 2 at various dopings. At finite

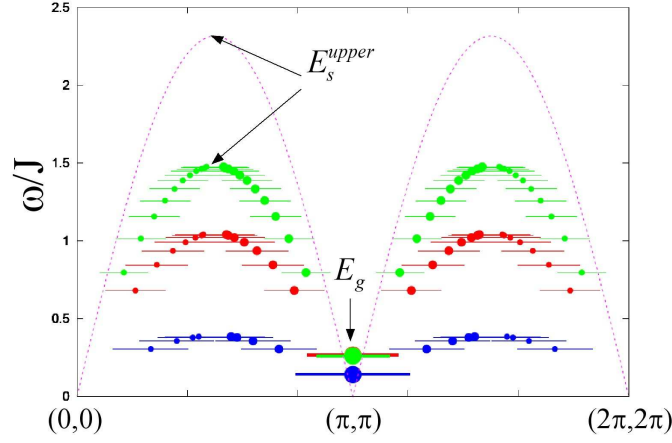


FIG. 2: Basic energy scales, E_s^{upper} and E_g , determined by the dynamic spin susceptibility function $\text{Im}\chi^{zz}(\mathbf{q}, \omega)$ at $T = 0$. The peak positions of $\text{Im}\chi^{zz}$ at $\delta = 0$ is shown in the energy and momentum (along the $q_x = q_y$ axis) by the dotted curve, which tracks the spin wave dispersion with $E_s^{\text{upper}} \simeq 2.3J$ and $E_g = 0$. The upper-bound energy E_s^{upper} monotonically decreases with increasing doping from 0.05, 0.125, to 0.2. E_g denotes the resonancelike peak energy at $\mathbf{q} = (\pi, \pi)$, which emerges in the LPP and SC state at finite doping. Note that the finite horizontal bars at finite doping indicate the momentum widths for these non-propagating modes.⁴²

doping, due to the opening up of the low-lying spin gap E_g , one finds a vanishing spectral weight of $\text{Im}D^{A^s}(\mathbf{q}, \omega)$ at $\omega < E_g$ and $T = 0$ according to Eq. (5). Since the spin gap E_g is directly related to the longest-size RVB pairs of spins, the effect of A^s , contributed by the π flux tubes bound to individual spinons in terms of Eq. (3), will get cancelled out cleanly in such a low-energy, long-wavelength regime. Consequently the bosonic holons in Eq. (1) will be free from the flux frustration and thus experience a Bose condensation at a sufficiently low temperature, which defines T_v for the LPP as previously stated. In fact, the zero-temperature spin dynamic susceptibility in Fig. 2 is obtained based on H_s under the holon condensation. Namely, the spin gap and holon condensation actually enforce each other self-consistently in the phase string model.

The gauge fluctuations in $D^{A^s}(\mathbf{q}, \omega)$ will gain a finite strength at $E_g \leq \omega \leq E_s^{\text{upper}}$ and then fall off rapidly beyond E_s^{upper} based on $\text{Im}\chi^{zz}(\mathbf{q}, \omega)$. At $\omega \gg E_s^{\text{upper}}$, the holons will mainly experience quasistatic gauge fluctuations concentrated at $\omega \lesssim E_s^{\text{upper}}$, with the total strength determined by

$$\langle (\Phi_{\square}^s)^2 \rangle = \int d\omega \frac{1}{N} \sum_{\mathbf{q}} 4\pi^2 S^{zz}(\mathbf{q}, \omega) \quad (6)$$

where $\Phi_{\square}^s = a^2 \hat{\mathbf{z}} \cdot (\nabla \times \mathbf{A}^s)$ defines the local flux per plaquette (surrounding a lattice site) and the spin structure factor $S^{zz}(\mathbf{q}, \omega) = \pi^{-1} [1 + n(\omega)] \text{Im}\chi^{zz}(\mathbf{q}, \omega)$. According to the sum rule discussed in Ref.⁴², one finds

$$\sqrt{\langle (\Phi_{\square}^s)^2 \rangle} \simeq \pi \sqrt{\frac{(3-\delta)(1-\delta)}{3}} \equiv |\Phi_{\square}^s|_{\text{max}} \quad (7)$$

In particular, if the temperature is further increased to $T \gtrsim T_0$, there is no more significant AF correlations among spins as $\Delta^s = 0$ such that (see Appendix A)

$$S^{zz}(\mathbf{q}, \omega) = \frac{1}{4\pi^2} |\Phi_{\square}^s|_{\text{max}}^2 \delta(\omega) \quad (8)$$

Then the corresponding gauge flux fluctuation becomes truly *static* with the weight $\sqrt{\langle (\Phi_{\square}^s)^2 \rangle}$ concentrating at $\omega = 0$.

Namely, the gauge field A^s simply describes the randomly distributed static flux at $T \geq T_0$ and quasistatic flux at high energy $\omega \gg E_s^{\text{upper}}$ in the case of $T < T_0$. Such regimes represent the maximal quantum frustration that the holons can experience in the phase string model governed by Eq. (1).

III. CHARGE DYNAMICS AT HIGH TEMPERATURE: TWO-COMPONENT FEATURE

In Sec. II C, we have seen that the strongest scattering to the charge carriers in the phase string model will set in at $T \geq T_0$ above the UPP, where the fluctuations of the gauge field \mathbf{A}^s are concentrated at $\omega = 0$, i.e., in the static limit. In the following we shall study the charge response as characterized by the optical conductivity and density-density correlation function in this regime. It has been noted that even at $T < T_0$, if $\omega \gg E_{\text{upper}}^s$, a quasi-static approximation for the gauge field A_{ij}^s should also be justified. In other words, the results obtained at $T \geq T_0$ should be still qualitatively applicable at $T < T_0$ at sufficiently *high energies*.

A. The density of states for holons

In the phase string model, the charge holons are coupled to the spin degrees of freedom via the topological gauge field A_{ij}^s defined in Eq. (3). Thus the charge dynamics is strongly influenced by the spin dynamics which decides the propagator of A_{ij}^s in terms of Eq. (5). As discussed in Sec. II C, the spin fluctuations are greatly reduced in the UPP at $T \geq T_0$ and become “static” [Eq. (8)] at the mean-field level as $\Delta^s = 0$. Accordingly, A_{ij}^s describes a static random flux at $T \geq T_0$ with the strength given by Eqs. (6) and (8).

Namely, above the UPP, the holons in H_h simply see a collection of $\pm\pi$ flux-tubes bound to spinons of number $(1-\delta)N$ which are de-paired ($\Delta^s = 0$) and randomly distributed in this regime with neglecting the spin-spin correlation at the mean-field level.

Then, at $T \geq T_0$ one can make a direct numerical simulation to diagonalize H_h for each random configuration of spinons like an impurity problem by a unitary transformation $h_i = \sum_m C_{im} a_m$ with C_{im} satisfying

$$-t_h \sum_{j=NN(i)} e^{iA_{ij}^s} C_{jm} = \varepsilon_m^h C_{im} \quad (9)$$

where $j = NN(i)$ denotes the four nearest neighbor sites. Note that the hard-core interaction between the holons is neglected here as we are mainly interested in the high-temperature or high-energy charge behavior below.

For the simplicity of numerical simulation, we define the smeared flux strength of A_{ij}^s on each *lattice* plaquette by

$$\sum_{\text{plaquette}} A_{ij}^s = \Phi_{\square} \quad (10)$$

and assume $\Phi_{\square} = \pm |\Phi_{\square}|_{\text{max}}$ with the signs $+$ and $-$ randomly distributed on the lattice plaquette and

$$|\Phi_{\square}|_{\text{max}} = (1 - \delta)\pi \quad (11)$$

Note that this assumption is valid when the individual π -flux tubes of total number of $1 - \delta$ spinons are well distinguished at high energy, short-distance scales, and $|\Phi_{\square}|_{\text{max}}$ is compatible in magnitude with $|\Phi_{\square}^s|_{\text{max}}$ in Eq. (7) of the mean-field version. But it should be emphasized that $|\Phi_{\square}|_{\text{max}}$ in Eq. (11) only provides an upper bound for the average flux strength per plaquette. One may think of many effects that can reduce its magnitude. For example, two flux tubes of opposite signs sitting at the nearest sites can partially cancel each other; the residual weak AF spin correlations among spinons will further enhance such cancellation; in addition, at larger doping the hopping of holons is always accompanied by a “backflow” of spinons which can mix $\pm\pi$ fluxes and reduce the average strength of $|\Phi_{\square}|$ from $|\Phi_{\square}|_{\text{max}}$.

Fig. 3 illustrates the holon density of states (DOS) obtained at $\delta = 0.125$ (solid curve). Here we have used the *quenched* method to average static random flux configurations of Φ_{\square} . The result shows how the DOS drastically reshaped by the gauge field, i.e., the *suppression* in the high-energy (mid-band) DOS, as compared to the flux free case (dashed curve). Note that the dotted curve in Fig. 3 represents the DOS for the case of a uniform π flux per plaquette, which looks similar to the present random flux case except that the momenta remains well defined in a reduced Brillouin zone in contrast to a strong mixing of momenta over a wide range by the scattering effect in the latter. By comparison, the DOS with a reduced $|\Phi_{\square}|_{\text{max}} = 0.4\pi$ (dash-dotted curve) is also presented. It is noted that other kinds of treatment for the static gauge field A_{ij}^s will generically lead to the similar overall behavior. For example, one may treat Φ_{\square} as a white-noise random flux distributed within the interval $[-|\Phi_{\square}|_{\text{max}}, +|\Phi_{\square}|_{\text{max}}]$ or even introduce some spatial correlation based on Eq. (5).

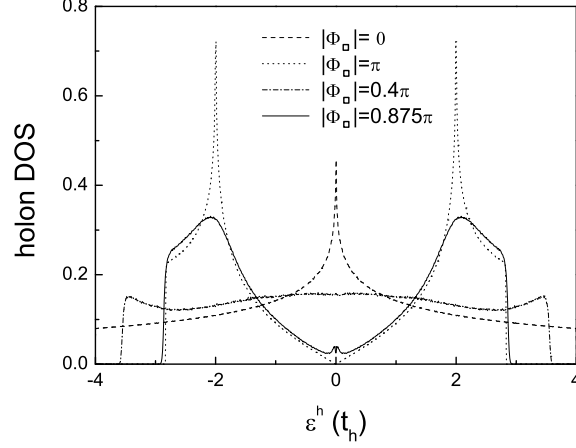


FIG. 3: Solid curve: the holon density of states (DOS) determined by H_h with the flux strength decided by Eq. (11) at $\delta = 0.125$ (see text) and the dash-dotted curve: with the reduced flux strength $|\Phi_\square| = 0.4\pi$. By comparison, the dashed curve represents the flux-free limit, while the dotted curve corresponds to the case in the presence of uniform π flux per plaquette. The calculation is done on a 32×32 lattice.

B. Optical conductivity: Two-component structure

Let us consider the optical conductivity using the Kubo formula

$$\sigma_{xx}(\mathbf{q} = \mathbf{0}, \omega) = \frac{i}{\omega} [\Pi_{xx}(\mathbf{q} = \mathbf{0}, \omega) - e^2 \langle T_x \rangle] \quad (12)$$

where $\Pi_{xx}(\mathbf{q} = \mathbf{0}, \omega) \equiv \Pi_{xx}(i\omega_n \rightarrow \omega + i0^+)$ is the retarded current-current correlation function with $\Pi_{xx}(i\omega_n) = -\int_0^\beta d\tau e^{i\omega_n \tau} \langle T_\tau J_x(\tau) J_x(0) \rangle$ and the charge current operator defined by

$$J_x(\mathbf{q}) = \frac{iet_h}{\sqrt{N}} \sum_i e^{-i\mathbf{q} \cdot \mathbf{r}_i} \left(h_{i+\hat{x}}^\dagger h_i e^{iA_{i+\hat{x},i}^s} - h_i^\dagger h_{i+\hat{x}} e^{iA_{i,i+\hat{x}}^s} \right) \quad (13)$$

$\langle T_x \rangle$ in Eq. (12) is defined by

$$\langle T_x \rangle = \frac{1}{N} \left\langle -t_h \sum_i e^{-i\mathbf{q} \cdot \mathbf{r}_i} \left(h_{i+\hat{x}}^\dagger h_i e^{iA_{i+\hat{x},i}^s} + h.c. \right) \right\rangle \quad (14)$$

The real part of the optical conductivity is then given by

$$\sigma'_{xx}(\omega) = \frac{\pi}{N} \sum_{m,m'} M_{mm'} \frac{n(\xi_m) - n(\xi_{m'})}{\xi_{m'} - \xi_m} \delta(\omega - \xi_{m'} + \xi_m) \quad (15)$$

in which $n(\xi_m) = 1/(e^{\beta\xi_m} - 1)$ is the Bose distribution factor with $\xi_m \equiv \varepsilon_m^h + \lambda_h$ and the matrix element

$$M_{mm'} \equiv e^2 t_h^2 \left| \sum_i (e^{iA_{i+x,i}^s} C_{i+x,m}^* C_{i,m'} - e^{iA_{i,i+x}^s} C_{i,m}^* C_{i+x,m'}) \right|^2 \quad (16)$$

with using Eq. (9) for a given static configuration of A_{ij}^s . Note that the final $\sigma'_{xx}(\omega)$ is obtained by averaging over the quenched random flux configurations as discussed above.

Fig. 4 shows the calculated real part of the optical conductivity at $\delta = 0.065$, with choosing the maximal flux strength in terms of Eq. (11). The main feature of the spectral curves at various temperatures $T \geq T_0$ is that they can all be decomposed into a two-component structure with a usual low-energy Drude component ($\sim 1/\omega^2$) and a mid-infrared resonancelike peak around the energy scale $\omega_{\text{mir}}^H \sim 4t_h$, with the whole spectrum eventually terminated below the energy $6t_h$.

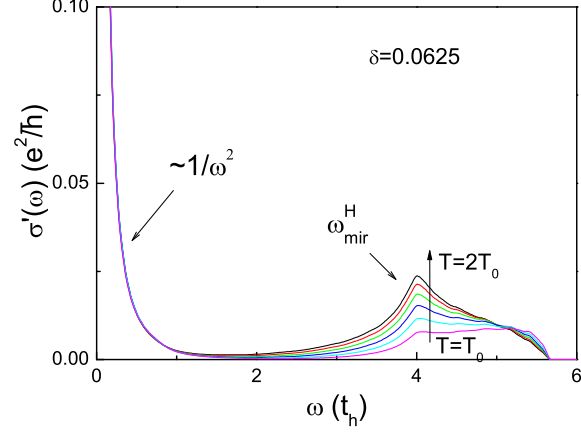


FIG. 4: The real part of the optical conductivity at $\delta = 0.0625$ with $|\Phi_\square| = |\Phi_\square|_{\max}$ and $T_0 \sim 0.5t_h$.

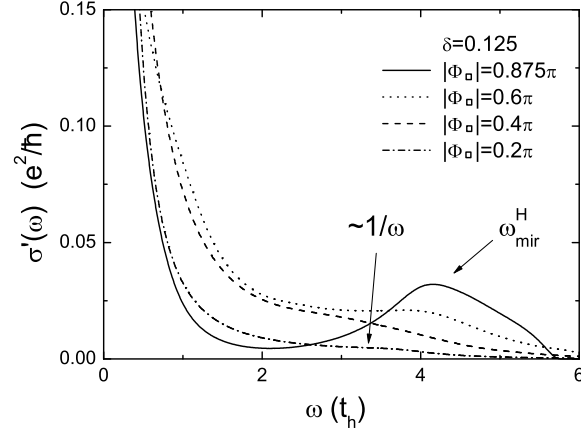


FIG. 5: The real part of the optical conductivity at $\delta = 0.125$ with $|\Phi_\square|$ chosen from $|\Phi_\square|_{\max} = 0.875\pi$ to 0.2π at a fixed $T = 0.5t_h$.

1. Mid-infrared peak

The origin of the mid-infrared resonance has been one of the most intriguing optical properties in the underdoped cuprates.^{1,2,5} Normally a photon with the momentum $\mathbf{q} \sim 0$ cannot excite a high-energy particle-hole pair involving a large momentum transfer due to the momentum conservation law, unless there is a scattering mechanism to strongly and widely smear the momentum. This is difficult to realize in a conventional electron-collective-mode coupling mechanism. The present model provides an alternative scattering mechanism due to the strong correlation effect caused by the on-site Coulomb repulsion in a doped Mott insulator.

We have already seen that the effect of A^s results in a double-peak structure in the holon DOS (Fig. 3). In contrast to the uniform π flux case shown in the same figure, which also has a double-peak structure, the high-energy inter-peak transition at $\mathbf{q} \rightarrow 0$ becomes possible in the random flux case due to the mixing between the small and large momenta by the strong scattering via A^s . This is the origin for the mid-infrared peak found in Fig. 4.

The presence of a peak in the optical conductivity around $\omega \sim 3t - 4t$ has been previously identified in the Hubbard and t - J models by exact numerical simulations^{27,46} Two approaches are consistent in this regard. Note that for such

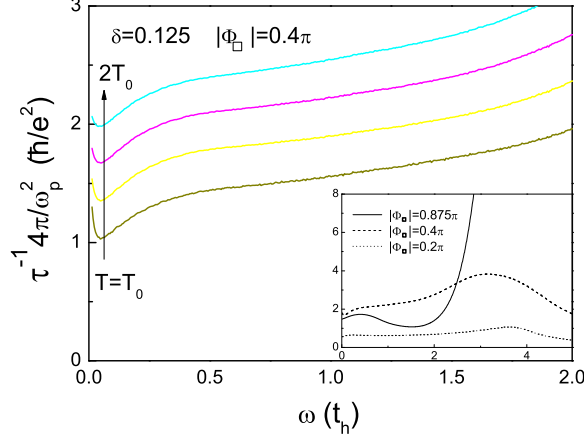


FIG. 6: The scattering rate $1/\tau(\omega)$ defined by Eq. (17) at various temperatures between $T_0 \simeq 0.25t_h$ and $2T_0$ which show a rough linear- ω dependence over a wide range at $\omega > k_B T_0$. Inset: $1/\tau(\omega)$ vs. ω at different $|\Phi_\square|$'s corresponding to Fig. 5.

a high-energy and short-distance physics the finite-size effect in the exact diagonalization calculation should not be important. In Sec. III C below, we shall further compare the density-density correlation function obtained by the exact diagonalization and present approach, where the ω -structures at different momenta can provide much richer features in further support of the consistency.

The above-discussed mid-infrared peak in the optical conductivity seems in contrast with the approximate $1/\omega$ behavior observed experimentally for the optimally and over-doped cuprates.⁵ But if one artificially reduces the magnitude $|\Phi_\square|$ from $|\Phi_\square|_{\max}$ given in Eq. (11), the mid-infrared peak will actually smoothly evolve into the $1/\omega$ behavior with reducing $|\Phi_\square|$, as clearly illustrated in Fig. 5 at a fixed holon concentration $\delta = 0.125$. In Fig. 5, the mid-infrared resonancelike peak at smaller $|\Phi_\square|$'s becomes softened and finally behaves like a $1/\omega$ tail in the regime $\sim 2t_h - 4t_h$ with the weight shifting towards the lower energy. As explained before, the strength of $|\Phi_\square|$ is expected to decrease faster with increasing doping than $|\Phi_\square|_{\max}$ given in Eq. (11). Such a picture is also consistent with the exact diagonalization calculations in the t - J model.⁴⁷

2. Low-energy component

Now let us closely examine the low- ω component of the optical conductivity. Experimentally the scattering rate is normally defined by

$$\frac{1}{\tau(\omega)} = \left(\frac{\omega_p^2}{4\pi} \right) \text{Re} \left[\frac{1}{\sigma(\omega)} \right] \quad (17)$$

which is determined by the measured optical conductivity. Here ω_p denotes the plasma frequency, which in the present case is given by $\omega_p = \sqrt{8\pi e^2 \delta t_h}$.

In Fig. 6, $1/\tau(\omega)$ based on the calculated $\sigma(\omega)$ is plotted as a function of ω in different temperatures at $\delta = 0.125$. Here we have chosen $|\Phi_\square| = 0.4\pi$ which corresponds to the case where the high- ω optical conductivity looks more like a $1/\omega$ behavior (Fig. 5). Here one finds that $1/\tau(\omega)$ increases monotonically with ω and is roughly linear- ω dependent over a wide ω region at $\omega > k_B T_0$. Note that generally the ω -dependence of $1/\tau(\omega)$ at higher energies is closely correlated with the evolution of the aforementioned mid-infrared feature, as shown in the inset of Fig. 6. Especially, as shown in the inset of Fig. 6, the non-monotonic behavior of $1/\tau(\omega)$ is also found in the strong gauge fluctuation case (e.g., $|\Phi_\square|_{\max} = 0.875\pi$), which corresponds to the heavily underdoped case, and is consistent with recent experimental results.^{2,5}

In particular, one sees a parallel shift of $1/\tau(\omega)$ with increasing temperature at low- ω in Fig. 6, which implies a linear-temperature dependence of the dc scattering rate. Such a parallel shift is also observed in the experiments^{10,48} which persists to a very high energy scale ($\sim 3000\text{cm}^{-1}$), implying an unconventional scattering mechanism in such

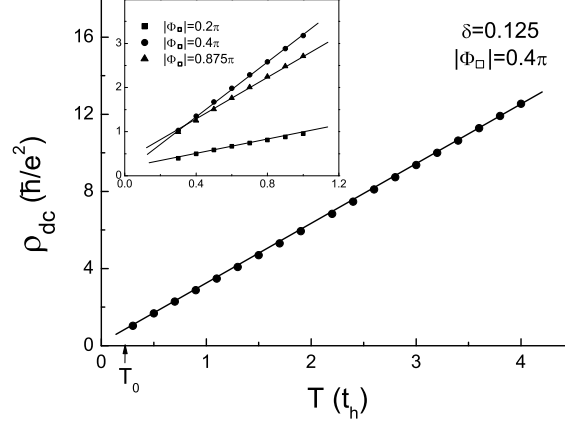


FIG. 7: The dc resistivity $\rho_{dc} = 1/\sigma'(\omega)|_{\omega \sim 0}$ as a function of temperature which is fit by a straight line showing the linear- T dependence. Inset: ρ_{dc} at different $|\Phi_{\square}|$'s which all show good linear- T behavior with slightly different slopes.

strongly correlated systems. The dc scattering rate $1/\tau_{dc}$ can be determined by extrapolating $1/\tau(\omega)$ to $\omega = 0$. Due to the parallel shift, the temperature dependence of $1/\tau(\omega)$ at low- ω is quite similar. The obtained dc resistivity based on the Drude formula $\rho_{dc} = (\omega_p^2/4\pi) \tau_{dc}^{-1} = 1/\sigma'(0)$ is shown in Fig. 7 which is indeed quite linear over a very wide range of temperature at $T \geq T_0$.

In order to understand the physical origin of the linear- T behavior, one may rewrite $\sigma'(0)$ in terms of Eq. (15) as follows

$$\sigma'(0) = \beta \frac{\pi}{N} \sum_m n(\xi_m) [1 + n(\xi_m)] \left[\sum_{m'} M_{mm'} \delta(\xi_m - \xi_{m'}) \right]$$

where the chemical potential λ_h in ξ_m is determined by $\sum_m n(\xi_m) = N\delta$. We find $\sigma'(0) \propto \beta$ over a very wide range of the temperature at $T > T_0$ where $n(\xi_m) \ll 1$, i.e., in the classical regime of the bosons. The corresponding scattering rate $\hbar/\tau_{dc} \sim 0.7k_B T$ for the case shown in the main panel of Fig. 7, whose slope is slightly $|\Phi_{\square}|$ dependent as indicated in the inset. Indeed, as discussed in Ref.³⁹, the bosonic degenerate regime already ends up at T_v , i.e., the boundary of the LPP/SVP (Fig. 1), where the excited spinon number becomes equal to the holon number such that the quantum phase coherence among the latter get totally interrupted by the former which carry π -flux tubes. At $T \geq T_0$, totally $1 - \delta$ randomly distributed π -flux tubes are perceived by δ holons and the latter behave like classical particles. One expects this anomalous transport be smoothly connected to the Brinkman-Rice retracing path regime⁴⁹ in the large T limit.

The dc scattering rate $\hbar/\tau_{dc} \sim 2k_B T$ has been previously obtained⁵⁰ by the quantum Monte Carlo numerical method, where the starting model is a system of interacting bosons coupled with strong Gaussian fluctuations of the static gauge field of the strength $\langle (\Phi_{\square}^s)^2 \rangle$. Note that $\langle (\Phi_{\square}^s)^2 \rangle$ used in the Monte Carlo simulation is about the same order of magnitude as in the above case and, in particular, it is temperature independent in contrast to the linear- T dependence predicted in the slave-boson U(1) gauge theory¹⁶ which was the original motivation for such a Monte Carlo study.⁵⁰ It is noted that the short-range repulsion between the holons has been taken into account in the Monte Carlo calculation, which may be responsible for the larger temperature slope of the scattering rate as compared to the present approach besides the Gaussian approximation used there. A further difference in the treatment is that we have used a quenched method to average over the static random flux configurations of Φ_{\square} since A_{ij}^s depicts π -flux tubes bound to random distributed spinons at $T \geq T_0$, while an *annealing* approximation is used in Ref.⁵⁰ because of the Gaussian fluctuations of the gauge flux employed there. As we are mainly interested in the high-temperature (or high-energy) behavior, such a difference is qualitatively not important as discussed in Ref.⁵¹.

It is noted that the lattice effect becomes very important at high-energy, short-distance at such strong flux fluctuations. It is actually responsible for the double-peak holon DOS, the mid-infrared feature in the optical conductivity, and the high- ω behavior of $1/\tau(\omega)$ discussed above. In the following we examine another consequence of this unique DOS structure.

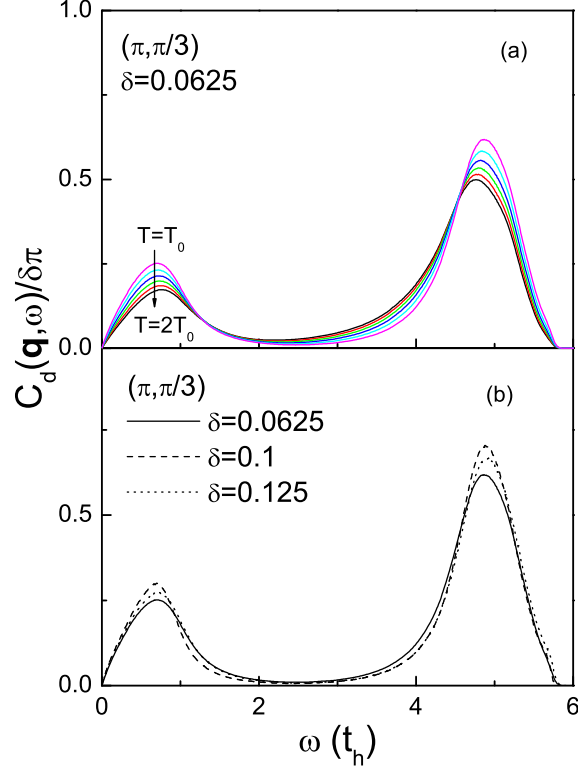


FIG. 8: (a) The density-density correlation function $C_d(\mathbf{q}, \omega)/\delta\pi$ at $\mathbf{q} = (\pi, \pi/3)$ at $\delta = 0.0625$ at various temperatures; (b) The scaling behavior of $C_d(\mathbf{q}, \omega)/\delta\pi$ at different dopings at $T = 0.5t_h$.

C. Density-density correlation function

In the above section, the mid-infrared resonance peak of the $\mathbf{q} = 0$ optical conductivity has been attributed to a large- ω transition between the double peaks of the holon DOS [Fig. 3], which is the consequence of the holon coupling with the strong fluctuating gauge field. In the following we discuss an independent probe of such a peculiar DOS structure by studying the density-density function at finite momentum \mathbf{q} and energy ω , and compare the results with the exact numerical calculations.

The charge (holon) number operator in the momentum space is expressed as

$$n(\mathbf{q}) = \sum_i e^{i\mathbf{q}\cdot\mathbf{r}_i} h_i^\dagger h_i \quad (18)$$

Similar to the (retarded) current-current correlation function, the imaginary part of the (retarded) density-density correlation function can be expressed as

$$C_d(\mathbf{q}, \omega) = \frac{\pi}{N} \sum_{m, m'} \left| \sum_i e^{i\mathbf{q}\cdot\mathbf{r}_i} C_{i, m}^* C_{i, m'} \right|^2 [n(\xi_m) - n(\xi_{m'})] \delta(\omega - \xi_{m'} + \xi_m)$$

Corresponding to the calculated optical conductivity in Figs. 4 and 5, using the same parameters and method, the structure function $C_d(\mathbf{q}, \omega)$ of the density-density correlation can be similarly computed.

The calculated $C_d(\mathbf{q}, \omega)/\delta\pi$ at momentum $\mathbf{q} = (\pi, \pi/3)$ are presented in Fig. 8 at different temperatures and doping concentrations. The double-peak structure as a function of ω reflects the underlying structure of the DOS of holons in Fig. 3 with $\Phi_\square = \pm |\Phi_\square|_{\max}$. An interesting feature shown in Fig. 8(b) is that $C_d(\mathbf{q}, \omega)/\delta\pi$ is roughly doping-independent. Such a “scaling” behavior was previously found numerically for the t - J model,³² which is generally

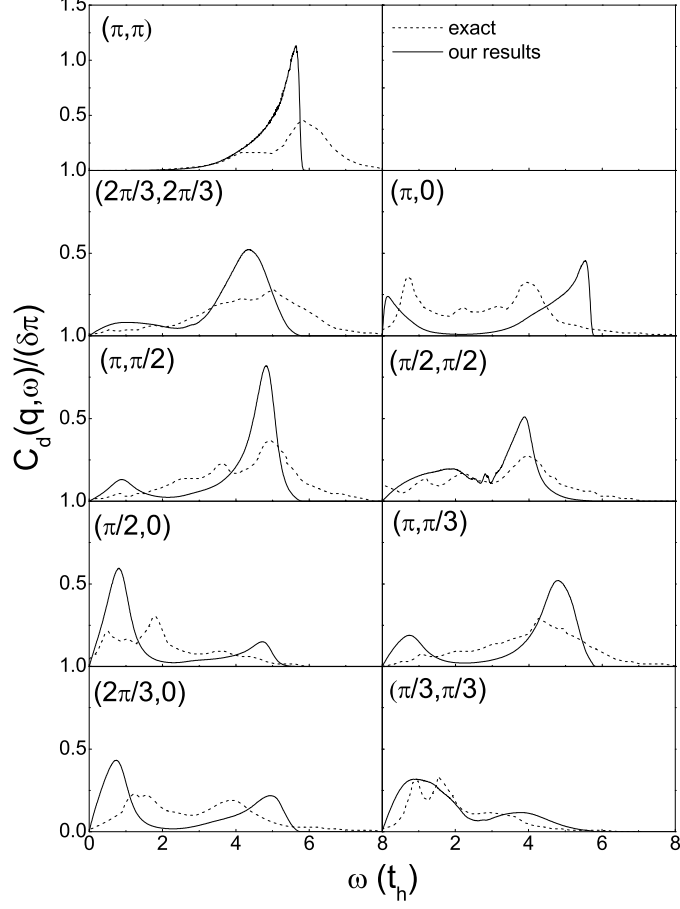


FIG. 9: The calculated density-density correlation function $C_d(\mathbf{q}, \omega)/\delta\pi$ at different momenta (solid curves) with $T = 0.5t_h$. The exact diagonalization results³² are shown as dashed curves.

inconsistent with the picture of particle-hole excitations in a Fermi liquid and was conjectured to be an indication of the bosonic description of charge excitations.³²

The calculated $C_d(\mathbf{q}, \omega)/\delta\pi$ is presented in Fig. 9 (solid curves), which evolves distinctively with different momenta. For comparison, the exact diagonalization results³² are presented as dotted curves. Due to the approximate doping-independence, the numerical result of four holes in a 4×4 lattice is used here. It is interesting to see that the overall ω -peak feature of the calculated density-density correlation function is in qualitative and systematic agreement with the numerical one at different \mathbf{q} 's without fitting parameters (here t is simply set at t_h as the mid-infrared feature peaks around $\sim 4t$ in the numerical calculation). Such a consistency between the present effective theory and the exact diagonalization provides another strong evidence, in addition to the mid-infrared resonance peak of the same origin, that the gauge-coupling boson model (1) correctly captures the high-energy charge excitations in the t - J model and large- U Hubbard model.

IV. LOW-ENERGY PSEUDOGAP BEHAVIOR AT LOW TEMPERATURE

So far we have been focused on the “normal state” above the UPP at $T \geq T_0$ where we have seen the maximal *static* scattering coming from the gauge field. As outlined in Sec. II, when the temperature decreases below T_0 , the spins start to form bosonic RVB pairs and develop short-range AF correlations. Although this does not change the overall integrated strength of the gauge fluctuations, due to the spin sum rule as given in Eqs. (6) and (7), the low- ω gauge fluctuations of \mathbf{A}^s will get suppressed progressively. Namely the scattering felt by the low-lying charge carriers

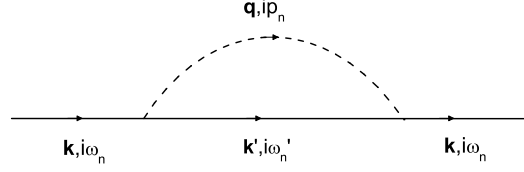


FIG. 10: Feynman diagram for the boson self-energy $\Sigma(\mathbf{k}, i\omega_n)$.

will be reduced. Here the gauge fluctuations are no longer static and are strongly correlated with the spin dynamics, where the above static approximation method is not applicable at least in the low-energy regime.

In the following we shall study the low-energy optical conductivity at $T < T_0$ by using the perturbative method and continuum approximation instead. Such an approach is meaningful in the regime where the spin fluctuations are substantially suppressed, which in turn results in the weak fluctuations of \mathbf{A}^s according to Eq. (5). Of course, as emphasized before, in the high-energy regime ($\omega \gg E_s^{\text{upper}}$) the charge carriers still feel the strong scattering by a quasistatic gauge fluctuation of the overall strength given by Eq. (7) and the previously results at $T \geq T_0$ are expected to still hold qualitatively.

A. Self-energy

In the case of weak gauge fluctuations, one can take the continuum limit in the Hamiltonian (1) as follows

$$H_h = -\frac{1}{2m_h} \int d^2\mathbf{r} h^\dagger(\mathbf{r}) [\nabla - i\mathbf{A}^s(\mathbf{r})]^2 h(\mathbf{r}) + \lambda_h \int d^2\mathbf{r} h^\dagger(\mathbf{r}) h(\mathbf{r}) \quad (19)$$

where $m_h = (2t_h a^2)^{-1}$ with a shift in the chemical potential $\lambda_h - 4t_h \rightarrow \lambda_h$. Further express $H_h = H_0 + H_1$ with

$$H_0 = \int \frac{d^2\mathbf{k}}{(2\pi)^2} \left(\frac{k^2}{2m_h} + \lambda_h \right) h_{\mathbf{k}}^\dagger h_{\mathbf{k}} \quad (20)$$

$$H_1 = -\frac{1}{2m_h} \left[\int \frac{d^2\mathbf{k}}{(2\pi)^2} \int \frac{d^2\mathbf{k}'}{(2\pi)^2} (\mathbf{k} + \mathbf{k}') \cdot \mathbf{A}^s(\mathbf{q}) + \int \frac{d^2\mathbf{q}_1}{(2\pi)^2} \mathbf{A}^s(\mathbf{q}_1) \cdot \mathbf{A}^s(\mathbf{q}_2) \right] h_{\mathbf{k}}^\dagger h_{\mathbf{k}'} \quad (21)$$

in which $\mathbf{q} = \mathbf{k} - \mathbf{k}'$ and $\mathbf{q}_1 + \mathbf{q}_2 = \mathbf{k} - \mathbf{k}'$.

We treat H_1 as a perturbation and calculate the holon self-energy up to the quadratic order of the gauge field. In the imaginary-time representation, the self-energy can be written as

$$\Sigma(\mathbf{k}, i\omega_n) = -\frac{1}{\beta(2m_h)^2} \sum_{ip_n} \int \frac{d^2\mathbf{k}'}{(2\pi)^2} G^{(0)}(\mathbf{k}', i\omega'_n) D_{\alpha\beta}^{A^s}(\mathbf{q}, ip_n) (\mathbf{k} + \mathbf{k}')^\alpha (\mathbf{k} + \mathbf{k}')^\beta \quad (22)$$

where the free boson field propagator $G^{(0)}(\mathbf{k}, i\omega_n) = 1/(\omega_n - \xi_{\mathbf{k}})$ with $\xi_{\mathbf{k}} = \frac{k^2}{2m_h} + \lambda_h$. The corresponding Feynman diagram is illustrated in Fig. 10 with $\mathbf{q} = \mathbf{k} - \mathbf{k}'$ and $p_n = \omega_n - \omega'_n$. By using the spectral function representation of D^{A^s} in terms of $\text{Im}\chi^{zz}$ according to Eq. (5) and after the frequency summation and analytic continuation $i\omega_n \rightarrow \omega + i0^+$, one finally obtains the imaginary part of the self-energy

$$\Sigma''(\mathbf{k}, \omega) = -\frac{4\pi^2}{(2m_h)^2} \int_{-\infty}^{\infty} d\omega' \int \frac{d^2\mathbf{k}'}{(2\pi)^2} \text{Im}\chi^{zz}(\mathbf{q}, \omega') \frac{|\mathbf{k} \times \mathbf{q}|^2}{q^4} [n(\xi_{\mathbf{k}'} + n(\omega') + 1] \delta(\omega - \xi_{\mathbf{k}'} - \omega') \quad (23)$$

Based on the dynamic spin susceptibility function $\text{Im}\chi^{zz}$ determined⁴² by H_s (see Appendix A), $\Sigma''(\mathbf{k}, \xi_{\mathbf{k}})$ can be then numerically computed and the results are presented in Fig. 11 at several low-temperatures below T_0 . It shows

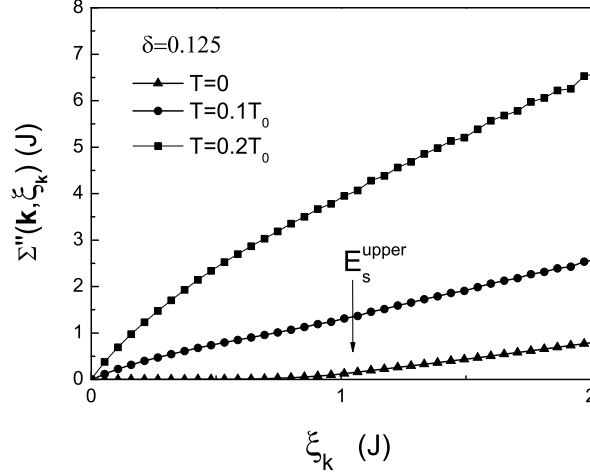


FIG. 11: The imaginary holon self-energy at various temperatures below T_0 .

that generally $\Sigma''(\mathbf{k}, \xi_{\mathbf{k}}) \propto \xi_{\mathbf{k}}$ at high energy with the slope dependent on temperature. But at low energy, $\Sigma''(\mathbf{k}, \xi_{\mathbf{k}})$ is quickly suppressed below E_s^{upper} at $T = 0$ or reduced from the linear- $\epsilon_{\mathbf{k}}^h$ behavior at finite temperature due to the presence of spin dynamics, characterized by $\text{Im}\chi^{zz}$ shown in Fig. 2, which makes the total strength of the gauge fluctuations spread over a finite ω region such that the effective scattering becomes weakened at low energy.

However, in contrast to a fermion system, the self-energy $\Sigma''(\mathbf{k}, \xi_{\mathbf{k}})$ is not generally related to the measurable transport properties for the present boson system. So in the follow we shall directly consider the optical conductivity based on the Kubo formula.

B. Optical conductivity

The optical conductivity $\sigma'(\omega)$ is determined by the retarded current-current correlation function. Note that in the continuum limit, the gauge-invariant current in the phase string model is given by

$$\mathbf{J} = -\frac{ie}{m_h} \int d^2r [h^\dagger(\mathbf{r}) \nabla h(\mathbf{r}) - i\mathbf{A}^s(\mathbf{r}) h(\mathbf{r})^\dagger h(\mathbf{r})] \quad (24)$$

which can be further written in two parts $\mathbf{J} = \mathbf{J}^A + \mathbf{J}^B$, with

$$\mathbf{J}^A = \frac{e}{m_h} \sum_{\mathbf{k}} \mathbf{k} h_{\mathbf{k}}^\dagger h_{\mathbf{k}} \quad (25)$$

$$\mathbf{J}^B = -\frac{e}{m_h \sqrt{Na}} \sum_{\mathbf{k}, \mathbf{q}} \mathbf{A}^s(\mathbf{q}) h_{\mathbf{k}+\mathbf{q}}^\dagger h_{\mathbf{k}} \quad (26)$$

Correspondingly, to leading order of approximation, the current-current correlation function contains two parts: $\Pi \equiv \Pi^A + \Pi^B$, where

$$\Pi^A(i\omega_n) = -\frac{e^2}{m_h^2 N a^2 \beta} \sum_{\mathbf{k}} k^2 \sum_{ip_n} G_h(\mathbf{k}, ip_n + i\omega_n) G_h(\mathbf{k}, ip_n) \quad (27)$$

$$\Pi^B(i\omega_n) = -\frac{2e^2}{m_h^2 N^2 a^4 \beta^2} \sum_{\mathbf{k}, \mathbf{q}} \sum_{ip_n, ip'_n} D^A{}^s(\mathbf{q}, ip'_n) G_h^{(0)}(\mathbf{k}, ip_n - i\omega_n) G_h^{(0)}(\mathbf{k} + \mathbf{q}, ip_n + ip'_n) \quad (28)$$

with $G(\mathbf{k}, i\omega_n) = 1/[\omega_n - \xi_{\mathbf{k}} - \Sigma(\mathbf{k}, i\omega_n)]$.

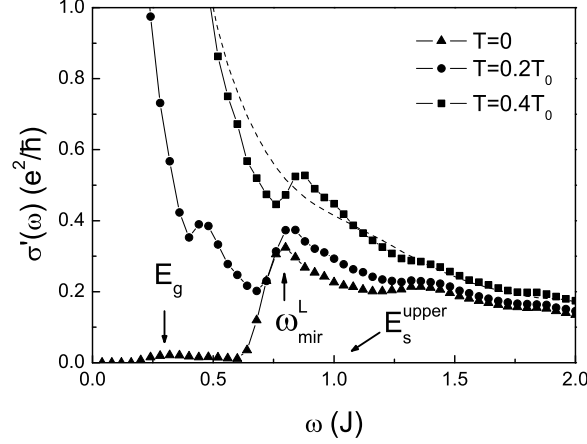


FIG. 12: Optical conductivity at different temperatures below T_0 . A new lower mid-infrared peak emerging at ω_{mir}^L which is weighted between the magnetic energy scales E_g and E_s^{upper} .

After the frequency summation and analytic continuation, one finds

$$\text{Im}\Pi^A(\omega) = -\frac{e^2}{2m_h^2 N a^2} \sum_{\mathbf{k}} k^2 \int_{-\infty}^{\infty} \frac{d\varepsilon}{2\pi} A_h(k, \varepsilon) A_h(k, \varepsilon + \omega) [n(\varepsilon) - n(\varepsilon + \omega)]$$

where the spectral function $A_h(\mathbf{k}, \omega)$ is defined as

$$A_h(\mathbf{k}, \omega) = \frac{-2\Sigma''(\mathbf{k}, \omega)}{[\omega - \xi_{\mathbf{k}} - \Sigma'(\mathbf{k}, \omega)]^2 + [\Sigma''(\mathbf{k}, \omega)]^2}$$

It is easy to find that without including $\Sigma(\mathbf{k}, \omega)$, $\text{Im}\Pi^A(\omega) = 0$ at finite ω . The behavior of $\Sigma''(\mathbf{k}, \omega)$ has been discussed in the last subsection. Its correction to $\text{Im}\Pi^A(\omega)$ turns out to be in a higher-order as compared to the leading contribution in $\text{Im}\Pi^B(\omega)$ given below

$$\begin{aligned} \text{Im}\Pi^B(\omega) &= \frac{2e^2}{m_h^2 N^2 a^4} \sum_{\mathbf{k}, \mathbf{q}} \int_0^{\infty} d\omega' \text{Im}D^{A^s}(q, \omega') [n(\xi_{\mathbf{k}}) - n(\xi_{\mathbf{k}+\mathbf{q}})] \{ [n(\omega - \omega') + n(\omega') + 1] \\ &\quad \times \delta(\omega - (\xi_{\mathbf{k}+\mathbf{q}} - \xi_{\mathbf{k}}) - \omega') + [n(\omega') - n(\omega + \omega')] \delta(\omega - (\xi_{\mathbf{k}+\mathbf{q}} - \xi_{\mathbf{k}}) + \omega') \} \end{aligned} \quad (29)$$

To study the low- ω behavior, thus one needs only to keep the second term: $\sigma'(\omega) \approx -\text{Im}\Pi^B(\omega)/\omega$. In Fig. 12, we have plotted the calculated optical conductivity at various low temperature below T_0 at $\delta = 0.125$. A prominent suppression of $\sigma'(\omega)$ at low- ω is present at $T = 0$ with a second “mid-infrared” peak emerging around $\omega_{\text{mir}}^L \sim 0.75J$ which sits somewhat between the two characteristic magnetic energy scales, E_g and E_s^{upper} , as marked in the figure. Note that such a new energy scale in the low- ω optical conductivity merely reflects some weighted energy scale based on the magnetic $\text{Im}\chi^{zz}$, which may be seen from the following simplified formula for the optical conductivity at low temperature

$$\sigma'(\omega) \simeq \frac{2\pi^2 e^2 N}{m_h^2 N^2 a^4 \omega} \sum_{\mathbf{q} \neq 0} \int_{-\infty}^{\infty} d\omega' \frac{1}{a^2 q^2} \text{Im}\chi^{zz}(q, \omega') (1 + n(\omega')) \delta(\omega - \xi_{\mathbf{q}} - \omega')$$

With the increase of temperature, the “gap” at low energy in $\sigma'(\omega)$ is quickly filled up by the thermal excitations as shown in Fig. 12. The lower “mid-infrared” peak feature remains around ω_{mir}^L at low temperature throughout the LPP below T_v . Note that T_v is between T_c and T_0 , and the dashed curve at $T = 0.4T_0$ is obtained by supposing that $T > T_v$ where $\text{Im}\chi^{zz}$ behaves differently.³⁸ As compared to the solid curve at the same $T = 0.4T_0$, which corresponds

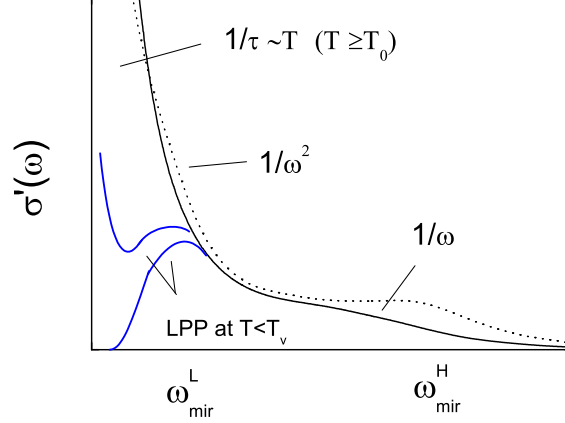


FIG. 13: A schematic optical conductivity summarizing the general behavior at different energy and temperature regimes in the phase string model.

to the case *inside* the LPP, the overall difference is small except for the vanishing the lower “mid-infrared” peak [Fig. 12].

Finally, we note that a Drude behavior without any signature of pseudogap feature is indeed recovered if the phase at $T \geq T_0$ is *extrapolated* to $T = 0$ with using Eq. (8):

$$\sigma'(\omega) \simeq -\frac{\text{Im}\pi_{xx}^B(\omega)}{\omega} \rightarrow \frac{\delta e^2 \langle (\Phi_{\square}^s)^2 \rangle}{2\omega^2/t_h^2} \quad (30)$$

Of course, the perturbative approach is no longer expected to work reliably at such strong flux fluctuations.

V. SUMMARY AND DISCUSSIONS

We have studied the charge dynamics based on the phase string model of the doped Mott insulator. This model possesses a mutual Chern-Simons gauge interaction between the bosonic holons and spinons, which is responsible for some highly non-trivial charge and spin dynamics in the system.

In the present work, the optical conductivity generally exhibits a two-component feature: a “coherent” low-energy part plus an “incoherent” high-energy part. The former is Drude-like at high temperature, which gradually gets suppressed, after entering the upper and lower pseudogap phases, at $\omega < \omega_{\text{mir}}^L$. This is related to the reduction of spin fluctuations, with a lower “mid-infrared” peak emerging at ω_{mir}^L in $\sigma'(\omega)$ which is originated from a weighted magnetic energy scale between E_g (associated with the resonancelike energy in the dynamic spin susceptibility) and E_s^{upper} (an upper bound magnetic energy for $S = 1$ excitations). The high-energy incoherent part shows a resonance around $\omega_{\text{mir}}^H \sim 4t_h$ if the gauge fluctuation is sufficiently strong, which can smoothly evolve into a $1/\omega$ tail at weak gauge fluctuations, consistent with the situations in underdoping and optimal/over-doping, respectively. The overall features of the optical conductivity are summarized in Fig. 13, whose behavior is specified by two energy scales: ω_{mir}^L and ω_{mir}^H , which have been observed⁷ experimentally. We have also shown that the high mid-infrared resonance at ω_{mir}^H can be closely correlated with the ω structure in the density-density correlation function which agrees qualitatively with the exact diagonalization results at all momenta.

The high-temperature Drude component is characterized by a linear- T scattering rate $1/\tau_{\text{dc}}$ in the region of $T > T_0$. This is consistent with the previous result obtained⁵⁰ using the quantum Monte Carlo simulation for a phenomenological model of repulsive bosons interacting with a strong spatially fluctuating gauge field. Furthermore, in the same high-temperature regime, the scattering rate $1/\tau(\omega)$ also shows an approximate linear ω dependence in the case when the high- ω optical conductivity evolves into a $1/\omega$ behavior. Thus, the phase string model can give a consistent explanation for the anomalous dc and ac transport in the normal state of the optimally doped high- T_c cuprates. Note that

such linear T or ω dependence of the scattering rate above the pseudogap phase is really a high temperature/energy behavior and thus is distinct from a quantum critical phenomenon.

Physically, the phase boundary at T_0 separates the high-temperature classical regime from the spin “degenerate regime” in the UPP where the spins form the RVB pairing with $\Delta^s \neq 0$. In the classical regime, both the charge and spin degrees of freedom behave diffusively, and the linear- T relaxation rate may be regarded as the system in the “quantum limit of dissipation”.⁵² It is interesting to see how small T_0 is as compared to a normal Fermi degenerate temperature scale. The charge holons will gain quantum coherence below a lower temperature T_v in the “boson degenerate regime” as illustrated in Fig. 1, where the optical conductivity exhibits the pseudogap behavior at low energy. Note that at $T \gtrsim T_0$, although $\Delta^s = 0$, the superexchange J still plays a critical role³⁵ to “repair” the spin “ \hat{z} -component mismatch” created by the hopping of the holes to ensure an effective hopping integral, while the “irreparable” transverse spin mismatch described by the phase string effect is responsible for the maximal gauge flux frustration discussed in this paper. Such a “normal state” is expected to be smoothly connected to the Brinkman-Rice retracable path limit⁴⁹ at $T \gg T_0$, where the role of J eventually diminishes and the present effective model is no longer valid.

Therefore, the simple boson model (1) seems to well capture many important high-energy properties of the charge excitations in the cuprates and the $t - J$ model. Another interesting channel to probe the high-energy spin-charge separation is the ARPES experiment. We expect to see the distinct energy scales in the single electron spectral function and a detailed study of the high-energy structure based on the phase string model will be presented elsewhere. It is further noted that in the present work we have not considered the quasiparticle contribution to the optical conductivity. In the phase string model, a spin-charge recombination will occur in the superconducting phase in which nodal quasiparticles become stable below the energy scale set by E_g .⁵³ But this is a fairly low energy as compared to ω_{mir}^L , which should not change the overall picture presented in Fig. 13.

APPENDIX A: SPIN DYNAMIC SUSCEPTIBILITY FUNCTION

According to Ref.⁴², the spinon Hamiltonian H_s in Eq. (2) can be diagonalized as $H_s = \sum_{m\sigma} E_m \gamma_{m\sigma}^\dagger \gamma_{m\sigma} + \text{const.}$ by the Bogoliubov transformation

$$b_{i\sigma} = \sum_m w_{m\sigma}(i) [u_m \gamma_{m\sigma} - v_m \gamma_{m-\sigma}^\dagger] \quad (\text{A1})$$

with the spinon wave function $\omega_{m\alpha}(i)$ determined by the eigen equation:

$$\xi_m \omega_{m\sigma}(i) = -J_s \sum_{j=nn(i)} e^{-i\sigma A_{ji}^h} \omega_{m\sigma}(j) \quad (\text{A2})$$

and

$$u_m = \frac{1}{\sqrt{2}} \sqrt{\frac{\lambda}{E_m} + 1} \quad (\text{A3})$$

$$v_m = \text{sgn}(\xi_m) \frac{1}{\sqrt{2}} \sqrt{\frac{\lambda}{E_m} - 1} \quad (\text{A4})$$

where the spinon excitation spectrum $E_m = \sqrt{\lambda^2 - \xi_m^2}$. Here the Lagrangian multiplier λ is determined by enforcing the average constraint $\langle \sum_\sigma b_{i\sigma}^\dagger b_{i\sigma} \rangle = 1 - \delta$, leading to

$$2 - \delta = \frac{1}{N} \sum_m \frac{\lambda}{E_m} \coth \frac{\beta E_m}{2} \quad (\text{A5})$$

Correspondingly the dynamic spin susceptibility function can be expressed as⁴²

$$\begin{aligned} \chi^{zz}(\mathbf{q}, i\omega_n) &= \frac{1}{N} \sum_{i,j} \int_0^\beta \langle S_i^z(\tau) S_j^z \rangle e^{-i\mathbf{q} \cdot (\mathbf{r}_i - \mathbf{r}_j) + i\omega_n \tau} d\tau \\ &= \frac{1}{4} \sum_{mm'\alpha} C_{mm'\alpha}(\mathbf{q}) \left[(u_m u_{m'} - v_m v_{m'})^2 \frac{n(E_{m'}) - n(E_m)}{i\omega_n + E_m - E_{m'}} \right. \\ &\quad \left. + (u_m v_{m'} - v_m u_{m'})^2 (1 + n(E_m) + n(E_{m'})) \times \frac{1}{2} \left(\frac{1}{i\omega_n + E_m + E_{m'}} - \frac{1}{i\omega_n - E_m - E_{m'}} \right) \right] \quad (\text{A6}) \end{aligned}$$

where $C_{mm'\alpha}(\mathbf{q}) = \frac{1}{N} \sum_{ij} e^{-i\mathbf{q} \cdot (\mathbf{r}_i - \mathbf{r}_j)} \omega_{m\alpha}^*(j) \omega_{m\alpha}(i) \omega_{m'\alpha}^*(i) \omega_{m'\alpha}(j)$. By taking the analytic continuation $i\omega_n \rightarrow \omega + i0^+$, one finally obtains

$$\begin{aligned} \text{Im}\chi^{zz}(\mathbf{q}, \omega) = & -\frac{\pi}{2} \sum_{mm'\alpha} C_{mm'\alpha}(\mathbf{q}) \{ (u_m u_{m'} - v_m v_{m'})^2 [n(E_{m'}) - n(E_m)] \delta(\omega + E_m - E_{m'}) \\ & + (u_m v_{m'} - v_m u_{m'})^2 [1 + n(E_m) + n(E_{m'})] \times \frac{1}{2} [\delta(\omega - E_m - E_{m'}) - \delta(\omega + E_m + E_{m'})] \} \end{aligned}$$

In the UPP at $T \geq T_0$, $J_s \rightarrow 0$ such that $E_m = \lambda$, $u_m = 1$ and $v_m = 0$. λ is determined by Eq. (A5) as³⁸ $e^{\beta\lambda} = (3 - \delta) / (1 - \delta)$. In this case, one finds the spin structure factor

$$\begin{aligned} S^{zz}(\mathbf{q}, \omega) &= \pi^{-1} [1 + n(\omega)] \text{Im}\chi^{zz}(\mathbf{q}, \omega) \\ &= \frac{1}{12} (3 - \delta) / (1 - \delta) \delta(\omega) \end{aligned} \quad (\text{A7})$$

which is concentrated at $\omega = 0$ as there is no spin-spin correlation at the mean-field level. Note that in obtaining the last line a correction factor $2/3$ is multiplied such that the precise sum rule $\int d\omega \sum_{\mathbf{q}} S^{zz}(\mathbf{q}, \omega) = N (S^z)^2 = N/4$ is satisfied at half-filling.⁴²

On the other hand, at $T = 0$, due to the holon condensation, A_{ji}^h can be treated as describing a uniform flux satisfying

$$\sum_{\text{plaquette}} A_{ij}^h = \delta\pi \quad (\text{A8})$$

which is expected to persist up to T_v . The detailed solution has been presented in Ref.⁴². In Fig. 2, the peak positions in $\text{Im}\chi^{zz}(\mathbf{q}, \omega)$ at different doping concentrations are shown.

ACKNOWLEDGMENTS

We would like to thank W. Q. Chen, D. K. K. Lee, V. N. Muthukumar, X. L. Qi, T. M. Rice, D. N. Sheng, J. Tu, and N. L. Wang for useful discussions. We also acknowledge stimulating discussions at Beijing Forum on High-Temperature Superconductivity, which led to the present work. This work has been partially supported by the NSFC grants.

-
- ¹ For a review, see D.B. Tanner and T. Timusk, in *Physical Properties of high temperature superconductors* edited by D. M. Ginsberg (World Scientific, Singapore, 1992), Vol. III, p.363.
- ² For a review, see D. N. Basov and T. Timusk, Rev. Mod. Phys. **77**, 721 (2005).
- ³ S. L. Cooper, D. Reznik, A. L. Kotz, M. A. Karlow, R. Liu, M. V. Klein, W. C. Lee, J. Giapintzakis, D. M. Ginsberg, B. W. Veal, and A. P. Paulikas, Phys. Rev. B **47**, 8233 (1993).
- ⁴ N. L. Wang, P. Zheng, T. Feng, G. D. Gu, C. C. Homes, J. M. Tranquada, B. D. Gaulin, and T. Timusk, Phys. Rev. B **67**, 134526 (2003).
- ⁵ Y. S. Lee, Kouji Segawa, Z. Q. Li, W. J. Padilla, M. Dumm, S. V. Dordevic, C. C. Homes, Yoichi Ando, and D. N. Basov, Phys. Rev. B **72**, 054529 (2005).
- ⁶ G. A. Thomas, D. H. Rapkine, S. L. Cooper, S-W. Cheong, A. S. Cooper, L. F. Schneemeyer, and J. V. Waszczak, Phys. Rev. B **45**, 2474 (1992).
- ⁷ G. A. Thomas, J. Orenstein, D. H. Rapkine, M. Capizzi, A. J. Millis, R. N. Bhatt, L. F. Schneemeyer, and J. V. Waszczak, Phys. Rev. Lett. **61**, 1313 (1988).
- ⁸ J. Hwang, T. Timusk, A. V. Puchkov, N. L. Wang, G. D. Gu, C. C. Homes, J. J. Tu, and H. Eisaki, Phys. Rev. B **69**, 094520 (2004).
- ⁹ J. J. Tu, C. C. Homes, G. D. Gu, D. N. Basov, and M. Strongin, Phys. Rev. B **66**, 144514 (2002).
- ¹⁰ J. Hwang, T. Timusk, and G. D. Gu, Nature **427**, 714 (2004).
- ¹¹ For reviews, see N. P. Ong, in *Physical Properties of high temperature superconductors* edited by D. M. Ginsberg, Vol. II, p. 459 (World Scientific, Singapore, 1990); Y. Iye, *ibid.*, Vol. III, p. 285 (1992).
- ¹² T. Nakano, M. Oda, C. Manabe, N. Momono, Y. Miura, and M. Ido, Phys. Rev. B **49**, 16000 (1994).
- ¹³ Yoichi Ando, Seiki Komiya, Kouji Segawa, S. Ono, and Y. Kurita, Phys. Rev. Lett. **93**, 267001 (2004).
- ¹⁴ C. M. Varma, P. B. Littlewood, S. Schmitt-Rink, E. Abrahams, and A. E. Ruckenstein, Phys. Rev. Lett. **63**, 1996 (1989).

- ¹⁵ P. W. Anderson, Nature Physics **2**, 626 (2006); P. W. Anderson, Phys. Rev. Lett., **64**, 1839 (1990).
- ¹⁶ P. A. Lee and N. Nagaosa, Phys. Rev. B **46**, 5621 (1992).
- ¹⁷ P. Monthoux and D. Pines, Phys. Rev. B **49**, 4261 (1994).
- ¹⁸ A. V. Chubukov, D. Pines, and J. Schmalian, in *The Physics of Superconductors*, edited by K. H. Bennemann and J. B. Ketterson (Springer, Berlin), Vol. 1, p. 495 (2003).
- ¹⁹ F. Marsiglio, T. Startseva, and J.P. Carbotte, Phys. Lett. A **245**, 172 (1998).
- ²⁰ J. P. Carbotte, E. Schachinger, and D.N. Bosov, Nature (London) **401**, 354 (1999).
- ²¹ A. Abanov, A.V. Chubukov, and J. Schmalian, Phys. Rev. B **63**, 180510(R) (2001).
- ²² N. L. Wang, P. Zheng, J. L. Luo, Z. J. Chen, S. L. Yan, L. Fang, and Y. C. Ma, Phys. Rev. B **68**, 054516 (2003).
- ²³ S. A. Trugman, Phys. Rev. B **37**, 1597 (1988).
- ²⁴ C. L. Kane, P. A. Lee, and N. Read, Phys. Rev. B **39**, 6880 (1989).
- ²⁵ S. Sachdev, Phys. Rev. B **39**, 12232 (1989).
- ²⁶ D. van der Marel, H. J. A. Molegraaf, J. Zaanen, Z. Nussinov, F. Carbone, A. Damascelli, H. Eisaki, M. Greven, P. H. Kes and M. Li, Nature **425**, 271 (2004).
- ²⁷ For a review, see Elbio Dagatto, Rev. Mod. Phys. **66**, 763 (1994).
- ²⁸ P. W. Anderson, Science **279**, **1196** (1998).
- ²⁹ Z. Zou and P. W. Anderson, Phys. Rev. B **37**, 627 (1988)
- ³⁰ T. Tohyama, P. Horsch, and S. Maekawa, Phys. Rev. Lett. **74**, 980 (1995).
- ³¹ B. O. Wells, Z.-X. Shen, A. Matsuura, D. M. King, M. A. Kastner, M. Greven, and R. J. Birgeneau, Phys. Rev. Lett. **74**, 964, (1995).
- ³² R. Eder, Y. Ohta, and S. Maekawa Phys. Rev. Lett. **74**, 5127 (1995).
- ³³ P. A. Lee and N. Nagaosa, Phys. Rev. B **46**, 5621 (1992).
- ³⁴ X. G. Wen and P. A. Lee, Phys. Rev. Lett. **76**, 503 (1996); P.A. Lee, N. Nagaosa, T.K. Ng, and X.-G. Wen, Phys. Rev. B **57**, 6003 (1998).
- ³⁵ Z. Y. Weng, D. N. Sheng, Y.-C. Chen, and C. S. Ting, Phys. Rev. B **55**, 3894 (1997).
- ³⁶ Z. Y. Weng, D. N. Sheng, C. S. Ting, Phys. Rev. Lett. **80**, 5401 (1998).
- ³⁷ Z. Y. Weng, Y. Zhou and V. N. Muthukumar, Phys. Rev. B **72**, 014503 (2005).
- ³⁸ Z. C. Gu and Z. Y. Weng, Phys. Rev. B **72**, 104520 (2005).
- ³⁹ Zheng-Yu Weng and Xiao-Liang Qi, Phys. Rev. B **74**, 144518 (2006); Z. Y. Weng and V. N. Muthukumar, *ibid*, **66**, 094509 (2002).
- ⁴⁰ Xiao-Liang Qi and Zheng-Yu Weng, cond-mat/0609525 (2006).
- ⁴¹ Su-Peng Kou and Zheng-Yu Weng, Phys. Rev. Lett. **90**, 157003 (2003).
- ⁴² W. Q. Chen and Z. Y. Weng Phys. Rev. B **71**, 134516 (2005).
- ⁴³ M. Shaw, Z. Y. Weng, and C. S. Ting, Phys. Rev. B **68**, 014511 (2003).
- ⁴⁴ J. M. Tranquada, cond-mat/0512115.
- ⁴⁵ Z. A. Xu, N.P. Ong, Y. Wang, T. Kakheshita, and S. Uchida, Nature, **406**, 486 (2000); Y. Wang, L. Li and N. P. Ong, Phys. Rev. B **73**, 024510 (2006).
- ⁴⁶ J. A. Riera and E. Dagatto, Phys. Rev. B **50**, 452 (1994).
- ⁴⁷ M. M. Zemljic and P. Prelovsek, Phys. Rev. B **72**, 075108 (2005).
- ⁴⁸ T. Startseva and T. Timusk, A. V. Puchkov, D. N. Basov, H. A. Mook, M. Okuya, T. Kimura, and K. Kishio, Phys. Rev. B **59**, 7184 (1999).
- ⁴⁹ W. F. Brinkman and T. M. Rice, Phys. Rev. B **2**, 1324 (1970).
- ⁵⁰ Don H. Kim, Derek K. K. Lee, and Patrick A. Lee, Phys. Rev. B **55**, 591 (1997).
- ⁵¹ M. U. Ubbens and P.A. Lee, Phys. Rev. B **49**, 13049 (1994).
- ⁵² J. Zaanen, Nature, **430**, 512 (2004).
- ⁵³ Z. Y. Weng, D. N. Sheng, and C. S. Ting, Phys. Rev. B **61**, 12328 (2000); Y. Zhou, V. N. Muthukumar, and Z. Y. Weng, Phys. Rev. B **67**, 064512 (2003).